Rapid Communications

Two phase transitions driven by surface electron doping in WTe_2

Antonio Rossi,[1,2] Giacomo Resta,[1] Seng Huat Lee,[3] Ronald Dean Redwing,[3] Chris Jozwiak,[2] Aaron Bostwick,[2] Eli Rotenberg,[2] Sergey Y. Savrasov,[1] and Inna M. Vishik[1,*]

[1]*Department of Physics, University of California, Davis, California 95616, USA*

[2]*Advanced Light Source, Lawrence Berkeley National Laboratory, Berkeley, California 94720, USA*

[3]*Materials Research Institute, Pennsylvania State University, University Park, Pennsylvania 16802, USA*

(Received 2 April 2020; accepted 15 September 2020; published 30 September 2020)

WTe_2 is a multifunctional quantum material exhibiting numerous emergent phases in which tuning of the carrier density plays an important role. Here, we demonstrate two nonmonotonic changes in the electronic structure of WTe_2 upon *in situ* electron doping. The first phase transition is interpreted in terms of a shear displacement of the top WTe_2 layer, which realizes a local crystal structure not normally found in bulk WTe_2. The second phase transition is associated with stronger interactions between the dopant atoms and the host, both through hybridization and electric field. These results demonstrate that electron doping can drive structural and electronics changes in bulk WTe_2 with implications for realizing nontrivial band-structure changes in heterointerfaces and devices.

DOI: 10.1103/PhysRevB.102.121110

Semimetallic two-dimensional (2D) materials, such as WTe_2, are characterized by numerous emergent electronic phenomena including large and nonsaturating magnetoresistance [1], superconductivity [2–5], and multiple topological phases [6–9]. They are also tunable via multiple perturbations including hydrostatic pressure [2], uniaxial strain [6], gating [4,5], alloying [10], doping [11], intercalation [3], THz and optical excitation [12,13], and preparation as monolayers [8,9]. Together, this creates an attractive platform for controlling many-body interactions, for realizing emergent heterointerface phenomena, and for switchable devices.

Carrier concentration plays a key role in the emergent phenomena of WTe_2. This material's large and nonsaturating magnetoresistance [1] has been attributed to perfect compensation of two electron and two hole pockets in the bulk electronic structure [14], albeit not without controversy [15–17]. As a consequence of this near balance of electrons and holes, the carrier concentration is also temperature dependent, yielding a Lifshitz transition ≈ 160 K [18] where the hole pockets are lost. Additionally, the onset of superconductivity under hydrostatic pressure [19] or potassium intercalation [3] in the bulk or with gating in the monolayer [4,5] is also associated with an excess of electronlike carriers. Although electron doping is not predicted to yield a structural phase transition, it is clear that it typically yields a different electronic ground state than the compensated system.

Here, we show that a small amount of surface electron doping in WTe_2 can induce a shear displacement in the top layer, producing a crystal structure locally similar to a polytype typically not encountered in ambient conditions. This phase transition is evidenced by pronounced changes in low-energy surface electronic structures with support from first-principles calculations. A second phase transition at higher doping levels affects higher-energy band structures, and is associated both with hybridization with dopant bands and the surface Stark effect. These results highlight the variety of electronic structure changes associated with electron doping in WTe_2, with implications for heterostructures and devices.

In the present angle-resolved photoemission spectroscopy (ARPES) experiments, *in situ* electron doping was achieved by depositing variable amounts of potassium on the cleaved WTe_2 surface (K dosing). ARPES experiments were performed at beamline 7.0.2 (MAESTRO) at the Advanced Light Source. The beam-spot size was $\approx 40\ \mu$m for the photon energies of 20 eV (Figs. 1 and 2) and 90 eV (Fig. 3). First-principles density function theory (DFT) calculations were performed using the localized pseudoatomic orbital method as implemented in OPENMX [20,21]. High-quality bulk single crystals of WTe_2 were synthesized by chemical vapor transport with bromine as the transport agent. More details about the experiment and computation are found in the Supplemental Material (SM) [22], which includes Refs. [23–34].

WTe_2 is a layered van der Waals (vdW) material consisting of stacked 2D sheets, and at ambient pressures the alignment between layers leads to a larger simple orthorhombic unit cell containing four formula units, called the γ or T_d phase [11,35,36]. This crystal structure breaks inversion symmetry along the c axis, giving rise to different surface bands on opposing sides of the material [37]. The different surfaces can be accessed by flipping a crystal over, and due to stacking faults, they can also be accessed with subsequent cleaves of a single orientation or different positions on an inhomogeneously cleaved surface [37]. The latter circumstance necessitates a sufficiently small ARPES beam spot to attain spectra on a single termination. Figures 1(b) and 1(c) highlight the two types of spectra present when different surfaces are exposed: Distinct bands are visible near $k_x = 0$ and $k_x = 0.25$, and in

*ivishik@ucdavis.edu

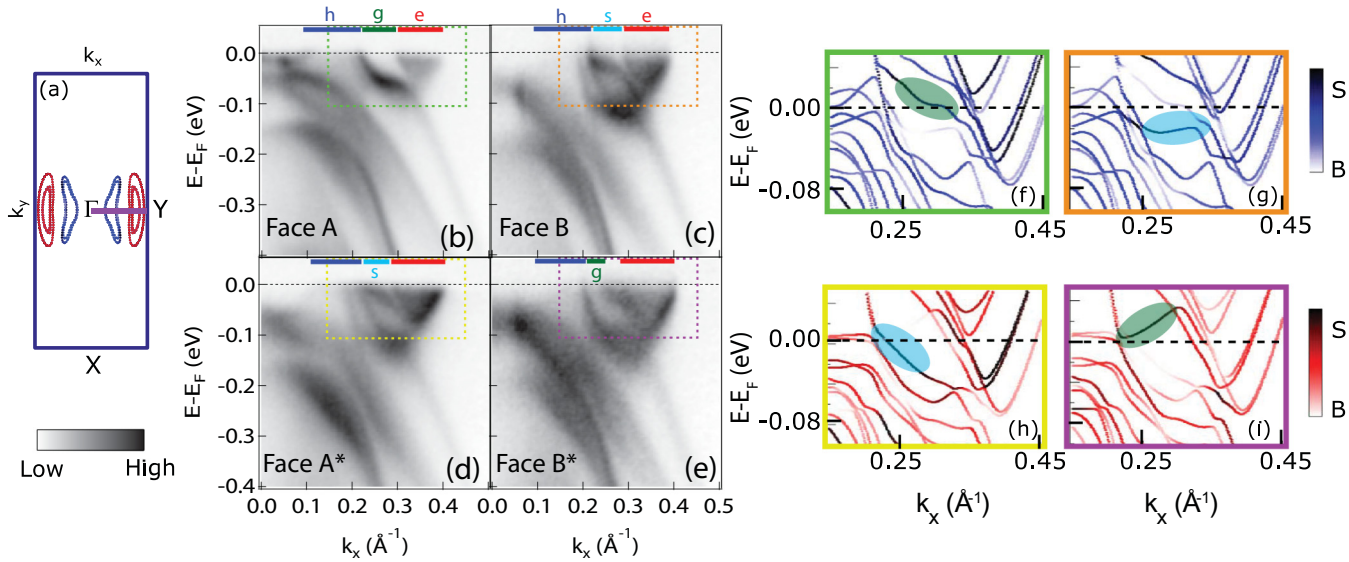

FIG. 1. First phase transition. (a) Schematic 2D projection of the Brillouin zone of WTe_2 with bulk electron (red) and hole (blue) Fermi surfaces. The magenta line is the Γ-Y cut. (b), (c) ARPES spectra taken on two opposite faces, along the Γ-Y direction, called faces A and B, respectively. (d), (e) Same cut after K dosing, called face A^* and B^*, respectively. Red, blue, green, and cyan bars mark the momentum region of electron (e), hole (h), gap (g), and surface (s) features. (f)–(i) DFT calculations in a region of the band structure indicated by the same color dashed boxes in (b)–(e). (f), (g) Calculations with the γ structure. (h), (i) Calculations with the β structure. The color scale indicates bands that are of surface (dark) vs bulk character (light). Green and cyan ovals indicate the changing surface band.

this Rapid Communication, we focus on the latter momentum region. Following the convention of Ref. [37], these surfaces are called face A and type B.

Figures 1(b)–1(e) show how *in situ* K dosing induces localized changes in the low-energy electronic structure on *both* nonequivalent crystalline faces of WTe_2, along a high-symmetry Γ-Y cut indicated in Fig. 1(a). Two electron pockets are resolved at $k_x \approx 0.3$–0.4, and a Fermi crossing of two hole bands can be seen near $k_x \approx 0.2$, either as two distinct bands (face B), or as a band and a shoulder (face A) [see Supplemental Material (SM) [22]]. Upon K dosing on face A [Figs. 1(b) and 1(d)], a new band appears in the gap between the electron and hole pockets, at $k_x \approx 0.25$, and the second hole band strengthens in intensity, though the latter is not the present focus. The opposite is observed for face B [Figs. 1(c) and 1(e)] where a band becomes less apparent and a gap emerges to the right of the hole pockets at a similar momentum. The nonequivalent faces of the K-dosed structure are referred to as A^* and B^*, respectively [Figs. 1(d) and 1(e)]. K dosing introduces a chemical potential shift of $\approx$0.03 eV or an electron doping of $\approx$3%–4% [22].

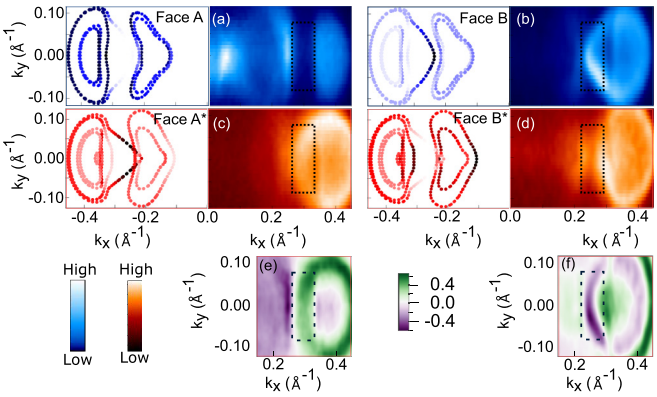

FIG. 2. Fermi-surface maps with corresponding DFT calculations mirrored across $k_x = 0$, before and after K dosing. (a), (b) Before dosing, faces A and B, with the corresponding DFT of the γ phase mirrored on left. (c), (d) After K dosing with the DFT of the β phase mirrored on the left. (e), (f) Difference spectra (A-A^*, B-B^*), where green (purple) indicates the spectral weight increase (decrease) upon dosing. In all panels, a dashed rectangle marks the momentum region of interest where the spectral weight increases (decreases) on face A^* (B^*).

DFT calculations [Figs. 1(f)–1(i)] are used to give a theoretical basis for the observed changes in the band structure, with the β ($1T'$) phase capturing the essential changes upon dosing. The changing portions of the calculated band structure are highlighted with shaded ovals. In the γ phase, the two faces differ via a surface-dominated band which is located above E_F on face A, hence not observable by ARPES, but below E_F on face B. The opposite is true for the β crystal structure where face A^* shows a surface-dominated band between the electron and hole pocket below E_F, but face B^* has this band above E_F. Most of the other bands in Fig. 1(b)–1(e) are changed minimally by doping. The structural change we propose is more subtle, and the comparison to the β phase will be justified later.

The appearance/attenuation of bands between the electron and hole pockets is highlighted further via evolving fermiology, shown in Fig. 2. Faces A and B differ by a segment of the Fermi surface extending from the electron to the hole pocket, present only on face B [Figs. 2(a) and 2(b)]. Earlier ARPES studies have demonstrated the 2D (surfacelike) nature of these states [37–39]. The present DFT calculations support the surface-dominated nature of the segments prominent on surface B. These surface states are sometimes misidentified

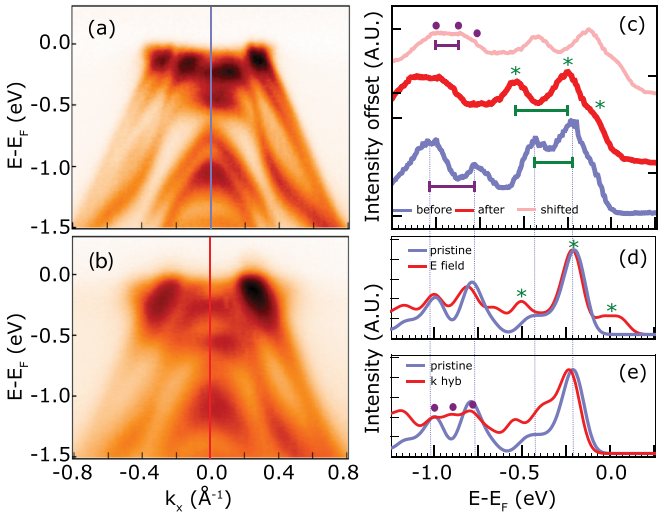

FIG. 3. Second phase transition with K dosing. (a) Γ-Y cut before dosing, (b) same cut after a large amount of dosing, and (c) energy distribution curve (EDC) at Γ comparing before (blue) and after (red) dosing. Pink EDC: "After" EDC with a 120 meV shift. Curves are offset vertically for clarity. Purple dots and green stars identify comparable features in all panels. Horizontal bars identify two sets of peaks before and after dosing, high energy (purple) and low energy (green). Thin vertical lines: Energy position of bands before dosing in experiment and calculations. (d) Slab calculations comparing "pristine" WTe_2 (γ phase, blue) to the effect of an electric field of 10 GV/m (red). (e) Slab calculations comparing "pristine" WTe_2 (blue) to the effect of hybridization with a K overlayer with one K atom per unit cell contributing 0.5 electrons (red). In (d) and (e), EDC broadening is produced by convolving calculated spectra with a Gaussian function which best reproduces the linewidth of data.

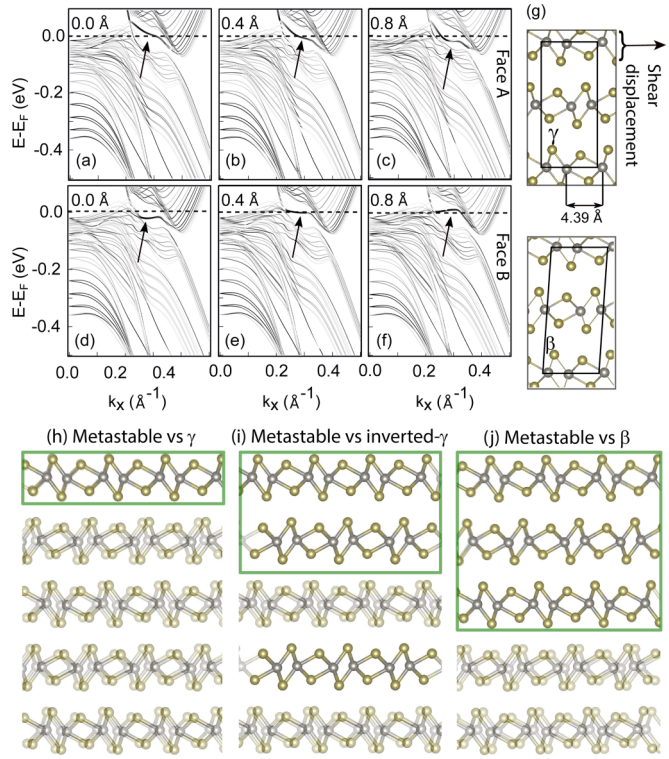

FIG. 4. First phase transition, DFT. (a)–(c) Slab calculations with different shear displacements of the top layer for face A termination. Darker (lighter) gray denotes a more surfacelike (bulklike) character. Arrows point to the surface-derived band that shifts with shear displacement. (d)–(f) Same for face B. (g) Definition of shear displacement in the γ unit cell, together with the β unit cell. (h)–(j) Overlay of metastable crystal structure (see text) with other crystal structures with a region of qualitative similarity indicated by a green box. (h) Overlay with γ. (i) Overlay with inverted γ, with opposite termination. (j) Overlay with β.

as the topological Fermi arcs in literature, but they do not connect surface projections of Weyl points and are therefore topologically trivial, though perhaps not irrelevant [7]. After K dosing, these surface states on surface B^* are less apparent [Fig. 2(d)], and a gap emerges between the electron and hole pockets (box) where the surface band previously connected the two. The opposite is seen on face A, where initially only electron and hole pockets are observed, but after dosing, new bands appear between them [Fig. 2(c)], whose DFT calculations for the β phase indicate to be surface states. This phenomenon on face A/A^* was previously reported, but not explained [40]. The doping-induced change is highlighted by subtracting normalized spectra from one another (A-A^*, B-B^*) in Figs. 2(e) and 2(f), where states near $k_x = 0.3$ are shown to appear (diminish) on face A (B). Notably, while an elevated temperature also diminishes the holelike bands, it does not appear to yield comparable changes in the surface bands between the electron and hole pockets [40–42].

Upon subsequent dosing cycles, the system undergoes a *second* phase transition (Fig. 3), corresponding to a chemical potential shift of ≈100–130 meV. The energy separation between bands changes significantly, particularly at the Γ point [Fig. 3(c)]. Four bands are resolved between the 0 and 1.25 eV binding energy (E_B), two at a lower E_B and two at a higher E_B. Initially, the two bands at lower E_B have an energy separation (Δ) of ≈220 meV, and after, they have $\Delta \approx 300$ meV (green bars). Additionally, a new shoulder appears at $E_B \approx 80$ meV. For the two bands resolved at higher E_B, initially $\Delta \approx 300$ meV, and afterwards, $\Delta \approx 170$ meV (purple bars). The second phase transition is also seen in the off-high-symmetry cuts, in the W and K core levels, and in the shape of the constant-energy maps at equivalent energies in the band structure, clarifying how the trivial effects of K dosing (rigid band shift and disorder broadening) differ from the present results [22]. The spectral changes at the Γ point for the second phase transition are compared to the effects of an electric field [Fig. 4(d)] and also to the effects of hybridization with a K overlayer [Fig. 4(e)], with qualitative agreement in different energy ranges.

The first phase transition manifests in changes in the surface bands at a low binding energy. Below, we will argue that this can be reproduced by a shear shift of the top WTe_2 layer for both terminations. We will also discuss the rationale for considering the β phase in DFT calculations in Figs. 1 and 2.

The γ to β transition can be visualized as shear displacements of subsequent layers, and the energy change when one WTe_2 layer is subjected to a variable amount of shear displacement is shown in SM [22] for bulk and slab geometry. A shear displacement of zero corresponds to the γ phase.

A shear displacement of ≈0.4 Å corresponds to a geometry where the Te atoms on adjacent layers are closest. For neutral or electron-doped WTe_2, repulsion of the Te antibonding orbitals leads to this configuration constituting a local maximum in energy and being unfavorable. Hole doping has the opposite effect, removing electrons from the Te antibonding orbitals and stabilizing this configuration. A displacement of ≈0.8 Å results in the Te atoms of adjacent layers adopting a locally mirrored configuration as compared to the WTe_2 γ state. With electron doping, a shear displacement of ≈0.8 Å corresponds to a *local* minimum in energy, and is referred to as a metastable configuration, while the global minimum is found at <-0.2 Å, very close to the γ configuration.

Although the metastable configuration is not a global energy minimum, the energy difference from the γ geometry is very small, <2 meV for one electron per unit cell. It should be noted that the DFT calculations cannot provide a reliable comparison of such small energy differences between the configurations, especially considering the difficulties in modeling the vdW interaction, such that the metastable configuration possibly has lower energy in the real system. Specifically, the electric field introduced by the ionization of the K atoms may favor this shear displacement [43].

In Figs. 4(a)–4(f), we consider how successive shear displacements of the top WTe_2 layer affect the band structure in the momentum region of interest. On surface *A*, the surface band located between the electron and hole pocket is initially above E_F and hence not observable by ARPES. It is gradually pushed below E_F by successive shear displacements of the top WTe_2 layer along the direction of the W-W zigzag chains. This band is fully below E_F and visible to ARPES between 0.6 and 0.8 Å. Thus the metastable configuration captures this key feature of the data and of the β-phase electronic structure. On face *B*, the opposite is observed, with a surface band initially below E_F between the electron and hole pockets, being pushed above E_F for a shear displacement between 0.6 and 0.8 Å. A full series of shear displacements is shown in SM [22].

We now discuss the similarity between the metastable configuration and other crystal structures [Figs. 4(h)–4(j)]. The metastable crystal structure is superimposed on top of the γ phase, the inverted γ phase (surface *A* and *B* reversed), and the β phase. Boxes denote regions of qualitative agreement. The metastable structure agrees qualitatively with the β structure in the first three layers, which explains why the two structures yield qualitatively similar surface bands. The comparison of ARPES data to the β-phase calculations is further justified by the surface sensitivity of the technique. For photoelectrons with a kinetic energy 20 eV, the mean free path is ≈6 Å [44], such that ≈99% of the photoemission signal comes from the first three WTe_2 layers. Additionally, the first two layers of the metastable structure agree well with the inverted γ structure, giving qualitative support for the observation that the electronic structures on the *A* and *B* surfaces seem to swap upon electron doping.

We now turn to the second phase transition, achieved with a large amount of K dosing, focusing on the Γ point where the largest spectral changes are observed. Qualitative comparisons are made with two scenarios that may both be present: hybridization between WTe_2 and the K overlayer and a surface dipole electric field produced between the electrons donated to WTe_2 and the positively charged K ions at the surface (surface Stark effect). In both cases, the upper limit of the physical values is considered, in order to highlight the effects of each phenomenon within the relatively complex band structure of WTe_2. The calculations do not consider the photoemission matrix element effects and thus do not aim to reproduce the relative heights of the peaks. The electric field qualitatively reproduces the results at a lower binding energy ($E_B < 0.6$ eV, green symbols). Before dosing, two bands are observed, and they move further apart at the second phase transition (green bars) with an additional shoulder developing at a lower binding energy. The surface Stark effect results in nonmonotonic band shifts depending on the orbital character, and has previously been demonstrated as a means of band gap engineering in semiconducting 2D materials [45–47]. Here, we indicate similar effects in a semimetallic 2D material. At a higher binding energy, a hybridization scenario better reproduces the observed effect of the dominant bands moving closer together (purple bars), and possibly exhibiting a third band as a shoulder feature (purple dots). We note that a monotonic chemical potential shift does not capture all observed spectral features (see SM [22]), which is why shifted (unshifted) spectra are used in qualitative comparisons to hybridization (electric field). These results highlight that band-structure changes may occur in heterointerfaces between WTe_2 and other 2D materials, which typically undergo a charge transfer because WTe_2 has a comparatively low work function among 2D materials [48].

In conclusion, we have demonstrated how surface electron doping can induce two distinct changes in the electronic structure of WTe_2. The first transition is interpreted in terms of a metastable shearing of the top WTe_2 layer, which yields surface bands qualitatively similar to the β phase within the first three layers. This also demonstrates how surface bands can identify subtle structural changes in WTe_2, which only minimally affect the bulk bands. Additionally, these results suggest that the same shear mode which has been proposed to be activated with hole doping and photoexcitation can also be activated with a very small amount of electron doping. The second phase transition reflects a more complicated interaction with the K atoms and host, involving both hybridization and the surface Stark effect. Both results are broadly relevant to understanding the effects of electrostatic gating, interactions with metallic contacts, and charge-transfer heterointerfaces in devices constructed from semimetallic 2D materials.

The authors acknowledge helpful discussions with Dr. Stiven Forti and Dr. Giuseppina Conti. I.V. and A.R. acknowledge support from UC Davis Startup funds and the Alfred P. Sloan Foundation (FG-2019-12170). Samples were provided by The Pennsylvania State University Two-Dimensional Crystal Consortium – Materials Innovation Platform (2DCC-MIP) which is supported by NSF Cooperative Agreement No. DMR-1539916. This research used resources of the Advanced Light Source, which is a U.S. Department of Energy Office of Science User Facility under Contract No. DE-AC02-05CH11231. G.R. and S.Y.S. were supported by National Science Foundation Grant No. DMR-1832728.

[1] M. N. Ali, J. Xiong, S. Flynn, J. Tao, Q. D. Gibson, L. M. Schoop, T. Liang, N. Haldolaarachchige, M. Hirschberger, N. P. Ong, and R. J. Cava, Nature (London) **514**, 205 (2014).

[2] X.-C. Pan, X. Chen, H. Liu, Y. Feng, Z. Wei, Y. Zhou, Z. Chi, L. Pi, F. Yen, F. Song, X. Wan, Z. Yang, B. Wang, G. Wang, and Y. Zhang, Nat. Commun. **6**, 7805 (2015).

[3] L. Zhu, Q.-Y. Li, Y.-Y. Lv, S. Li, X.-Y. Zhu, Z.-Y. Jia, Y. B. Chen, J. Wen, and S.-C. Li, Nano Lett. **18**, 6585 (2018).

[4] V. Fatemi, S. Wu, Y. Cao, L. Bretheau, Q. D. Gibson, K. Watanabe, T. Taniguchi, R. J. Cava, and P. Jarillo-Herrero, Science **362**, 926 (2018).

[5] E. Sajadi, T. Palomaki, Z. Fei, W. Zhao, P. Bement, C. Olsen, S. Luescher, X. Xu, J. A. Folk, and D. H. Cobden, Science **362**, 922 (2018).

[6] A. A. Soluyanov, D. Gresch, Z. Wang, Q. Wu, M. Troyer, X. Dai, and B. A. Bernevig, Nature (London) **527**, 495 (2015).

[7] Z. Wang, B. J. Wieder, J. Li, B. Yan, and B. A. Bernevig, Phys. Rev. Lett. **123**, 186401 (2019).

[8] S. Tang, C. Zhang, D. Wong, Z. Pedramrazi, H.-Z. Tsai, C. Jia, B. Moritz, M. Claassen, H. Ryu, S. Kahn, J. Jiang, H. Yan, M. Hashimoto, D. Lu, R. G. Moore, C.-C. Hwang, C. Hwang, Z. Hussain, Y. Chen, M. M. Ugeda, Z. Liu, X. Xie, T. P. Devereaux, M. F. Crommie, S.-K. Mo, and Z.-X. Shen, Nat. Phys. **13**, 683 (2017).

[9] X. Qian, J. Liu, L. Fu, and J. Li, Science **346**, 1344 (2014).

[10] T.-R. Chang, S.-Y. Xu, G. Chang, C.-C. Lee, S.-M. Huang, B. Wang, G. Bian, H. Zheng, D. S. Sanchez, I. Belopolski, N. Alidoust, M. Neupane, A. Bansil, H.-T. Jeng, H. Lin, and M. Zahid Hasan, Nat. Commun. **7**, 10639 (2016).

[11] H.-J. Kim, S.-H. Kang, I. Hamada, and Y.-W. Son, Phys. Rev. B **95**, 180101(R) (2017).

[12] E. J. Sie, C. M. Nyby, C. D. Pemmaraju, S. J. Park, X. Shen, J. Yang, M. C. Hoffmann, B. K. Ofori-Okai, R. Li, A. H. Reid, S. Weathersby, E. Mannebach, N. Finney, D. Rhodes, D. Chenet, A. Antony, L. Balicas, J. Hone, T. P. Devereaux, T. F. Heinz, X. Wang, and A. M. Lindenberg, Nature (London) **565**, 61 (2019).

[13] P. Hein, S. Jauernik, H. Erk, L. Yang, Y. Qi, Y. Sun, C. Felser, and M. Bauer, Nat. Commun. **11**, 2613 (2020).

[14] I. Pletikosić, M. N. Ali, A. V. Fedorov, R. J. Cava, and T. Valla, Phys. Rev. Lett. **113**, 216601 (2014).

[15] S. Thirupathaiah, R. Jha, B. Pal, J. S. Matias, P. K. Das, P. K. Sivakumar, I. Vobornik, N. C. Plumb, M. Shi, R. A. Ribeiro, and D. D. Sarma, Phys. Rev. B **95**, 241105(R) (2017).

[16] Y. Wang, K. Wang, J. Reutt-Robey, J. Paglione, and M. S. Fuhrer, Phys. Rev. B **93**, 121108(R) (2016).

[17] C.-L. Wang, Y. Zhang, J.-W. Huang, G.-D. Liu, A.-J. Liang, Y.-X. Zhang, B. Shen, J. Liu, C. Hu, Y. Ding, D.-F. Liu, Y. Hu, S.-L. He, L. Zhao, L. Yu, J. Hu, J. Wei, Z.-Q. Mao, Y.-G. Shi, X.-W. Jia *et al.*, Chin. Phys. Lett. **34**, 097305 (2017).

[18] Y. Wu, N. H. Jo, M. Ochi, L. Huang, D. Mou, S. L. Bud'ko, P. C. Canfield, N. Trivedi, R. Arita, and A. Kaminski, Phys. Rev. Lett. **115**, 166602 (2015).

[19] D. Kang, Y. Zhou, W. Yi, C. Yang, J. Guo, Y. Shi, S. Zhang, Z. Wang, C. Zhang, S. Jiang, A. Li, K. Yang, Q. Wu, G. Zhang, L. Sun, and Z. Zhao, Nat. Commun. **6**, 7804 (2015).

[20] T. Ozaki and H. Kino, Phys. Rev. B **69**, 195113 (2004).

[21] T. Ozaki, H. Kino, J. Yu, M. J. Han, N. Kobayashi, M. Ohfuti, F. Ishii, T. Ohwaki, H. Weng, and K. Terakura, http://www.openmx-square.org/.

[22] See Supplemental Material at http://link.aps.org/supplemental/10.1103/PhysRevB.102.121110 for experimental and computational details, additional DFT calculations and photoemission data.

[23] J. P. Perdew, K. Burke, and M. Ernzerhof, Phys. Rev. Lett. **77**, 3865 (1996).

[24] N. Troullier and J. L. Martins, Phys. Rev. B **43**, 1993 (1991).

[25] A. Damascelli, Z. Hussain, and Z.-X. Shen, Rev. Mod. Phys. **75**, 473 (2003).

[26] L.-G. Petersson and S.-E. Karlsson, Phys. Scr. **16**, 425 (1977).

[27] M. Cardona and L. Ley, *Photoemission in Solids I. General Principles*, Topics in Applied Physics Vol. 26 (Springer, Berlin, 1978).

[28] G. Broden and H. Bonzel, Surf. Sci. **84**, 106 (1979).

[29] K. Ozawa, T. Anazawa, S. Tokumitsu, R. Sekine, E. Miyazaki, K. Edamoto, S. Tanaka, and S. Otani, Surf. Sci. **336**, 93 (1995).

[30] M. Trioni, S. Achilli, and E. Chulkov, Prog. Surf. Sci. **88**, 160 (2013).

[31] Y. Wang, J. Xiao, H. Zhu, Y. Li, Y. Alsaid, K. Y. Fong, Y. Zhou, S. Wang, W. Shi, Y. Wang, A. Zettl, E. J. Reed, and X. Zhang, Nature (London) **550**, 487 (2017).

[32] B. E. Brown, Acta Crystallogr. **20**, 268 (1966).

[33] A. Mar, S. Jobic, and J. A. Ibers, J. Am. Chem. Soc. **114**, 8963 (1992).

[34] The ELK code, http://elk.sourceforge.net/.

[35] J. Augustin, V. Eyert, T. Böker, W. Frentrup, H. Dwelk, C. Janowitz, and R. Manzke, Phys. Rev. B **62**, 10812 (2000).

[36] W. G. Dawson and D. W. Bullett, J. Phys. C: Solid State Phys. **20**, 6159 (1987).

[37] F. Y. Bruno, A. Tamai, Q. S. Wu, I. Cucchi, C. Barreteau, A. de la Torre, S. McKeown Walker, S. Riccò, Z. Wang, T. K. Kim, M. Hoesch, M. Shi, N. C. Plumb, E. Giannini, A. A. Soluyanov, and F. Baumberger, Phys. Rev. B **94**, 121112(R) (2016).

[38] Y. Wu, D. Mou, N. H. Jo, K. Sun, L. Huang, S. L. Bud'ko, P. C. Canfield, and A. Kaminski, Phys. Rev. B **94**, 121113(R) (2016).

[39] J. Sánchez-Barriga, M. G. Vergniory, D. Evtushinsky, I. Aguilera, A. Varykhalov, S. Blügel, and O. Rader, Phys. Rev. B **94**, 161401(R) (2016).

[40] Q. Zhang, Z. Liu, Y. Sun, H. Yang, J. Jiang, S.-K. Mo, Z. Hussain, X. Qian, L. Fu, S. Yao, M. Lu, C. Felser, B. Yan, Y. Chen, and L. Yang, Phys. Status Solidi RRL **11**, 1700209 (2017).

[41] C. Wang, Y. Zhang, J. Huang, S. Nie, G. Liu, A. Liang, Y. Zhang, B. Shen, J. Liu, C. Hu, Y. Ding, D. Liu, Y. Hu, S. He, L. Zhao, L. Yu, J. Hu, J. Wei, Z. Mao, Y. Shi, X. Jia, F. Zhang, S. Zhang, F. Yang, Z. Wang, Q. Peng, H. Weng, X. Dai, Z. Fang, Z. Xu, C. Chen, and X. J. Zhou, Phys. Rev. B **94**, 241119(R) (2016).

[42] S. Thirupathaiah, R. Jha, B. Pal, J. S. Matias, P. K. Das, I. Vobornik, R. A. Ribeiro, and D. D. Sarma, Phys. Rev. B **96**, 165149 (2017).

[43] Q. Yang, M. Wu, and J. Li, J. Phys. Chem. Lett. **9**, 7160 (2018).

[44] M. P. Seah and W. A. Dench, Surf. Interface Anal. **1**, 2 (1979).

[45] M. Kang, B. Kim, S. H. Ryu, S. W. Jung, J. Kim, L. Moreschini, C. Jozwiak, E. Rotenberg, A. Bostwick, and K. S. Kim, Nano Lett. **17**, 1610 (2017).

[46] Z. Zhang, Z. Chen, M. Bouaziz, C. Giorgetti, H. Yi, J. Avila, B. Tian, A. Shukla, L. Perfetti, D. Fan, Y. Li, and A. Bendounan, ACS Nano **13**, 13486 (2019).

[47] K. Fukutani, R. Stania, J. Jung, E. F. Schwier, K. Shimada, C. I. Kwon, J. S. Kim, and H. W. Yeom, Phys. Rev. Lett. **123**, 206401 (2019).

[48] Y. Liu, P. Stradins, and S.-H. Wei, Sci. Adv. **2**, e1600069 (2016).